Phonon transmission at crystalline-amorphous interfaces studied using mode-resolved atomistic Green's functions

Lina Yang, Benoit Latour, and Austin J. Minnich[*]

Division of Engineering and Applied Science, California Institute of Technology, Pasadena, California 91125, USA

The transmission and reflection processes of THz phonons at solid interfaces are of fundamental interest and of importance to thermal conduction in nanocrystalline solids. The processes are challenging to investigate, however, because typical experiments and many computational approaches do not provide transmission coefficients resolved by phonon mode. Here, we examine the modal transmission and reflection processes of THz phonons across an amorphous Si region connected to two crystalline Si leads, a model interface for those that occur in nanocrystalline solids, using mode-resolved atomistic Green's functions. We find that the interface acts as a low-pass filter, reflecting modes of frequency greater than around 3 THz while transmitting those below this frequency, in agreement with a recent experimental report [C. Hua *et al.*, Phys. Rev. B **95**, 205423 (2017)]. Further, we find that these low frequency modes travel nearly unimpeded through the interface, maintaining their wave vectors on each side of the interface. Our work shows that even completely disordered regions may not be effective at reflecting THz phonons, with implications for efforts to alter thermal conductivity in nanocrystalline solids.

I. INTRODUCTION

Solid interfaces play a key role in the thermal properties of nanostructured materials due to their contribution to the overall thermal resistance of the solid [1,2]. With sufficient interface density, this thermal boundary resistance (TBR) can dominate the total thermal resistance, leading to solids with exceptionally low thermal conductivity [3]. TBR is the average result of transmission and reflection of phonons over the entire Brillouin zone by the interface. Creating materials with extreme thermal properties thus requires a fundamental understanding of these processes.

This understanding is difficult to achieve, however, due to limitations in experimental and computational approaches in accessing information on transmission processes resolved by mode. The most common experimental approach to measure TBR, time-domain thermoreflectance, provides only the total TBR, obscuring these microscopic processes [4]. The most widely used simplified models for phonon transmission at an interface, the acoustic mismatch model (AMM) in the long wavelength limit [5] and the diffuse mismatch model (DMM) in the short wavelength limit [3], fail to explain many experimental observations and cannot account for the atomic structure of the interface [5]. Molecular dynamics (MD) simulations allow the overall value of the TBR to be computed [6–11], and recent works also provide frequency and mode-resolved information on interfacial heat flux [12–16]. The phonon wave-packet method, which is a mode-resolved technique based on MD, can predict interface thermal conductance by tracking the transmitted and reflected energy including full anharmonicity of the interaction potentials, but

it is computationally expensive and difficult to apply to oblique angles [17,18]. Lattice dynamics is another atomistic method to compute the interface thermal conductance by solving for the transmitted and reflected wave functions given the boundary conditions at the interfaces, but it can be difficult to implement for interfaces with complex atomic structure [19,20].

Compared to wave packet and lattice dynamics methods, the atomistic Green's function (AGF) method is more efficient and easier to implement, and it has been used extensively to compute the frequency dependent transmission through a device connected to reservoirs [21–26]. Such quantum transport problems have been studied by the quantum transmitting boundary method (QTBM) [27] and the nonequilibrium Green's function (NEGF) method [28], which provide general framework for electron transport and the modeling of physics of nanoscale devices [29]. Phonon transport across a mismatched Si/Ge interface was studied by Li and Yang using a recursive AGF method, who found that lattice mismatch increases the lattice disorder, which in turn decreases interface thermal conductance [30]. Tian *et al.* examined the impact of interface roughness on phonon transmission due to atomic mixing [31]. However, the forms of AGF used in these studies resolve phonon transmission only by frequency, not by mode.

Recently, Ong and Zhang extended the conventional AGF formalism to mode-resolved AGF to calculate phonon modal transmission and applied it to a graphene/boron-nitride interface [32]. We recently used this method to examine mode-resolved phonon transmission at crystalline Si/Ge interfaces [33]. A similar numerical method has also been developed using perfectly matched layer boundaries to compute mode-resolved transmission [34]. Sadasivam *et al.* extended the conventional AGF technique to eigenspectrum-based AGF, and they found that phonon transmission is enhanced in Si/Ge interfaces with atomic intermixing due to the increased phase

---

*Corresponding author: aminnich@caltech.edu

space available for phonon mode conversion [35]. However, mode-resolved AGF has not been applied to amorphous Si (aSi) interfaces with three-dimensional solids that are present in actual nanocrystalline solids.

Here, we report a study of phonon transmission using the mode-resolved AGF across an aSi interface between two crystalline Si (cSi) leads. We find that the interface acts as a low-pass filter, reflecting modes of frequency greater than around 3 THz while transmitting those below this frequency, in agreement with a recent experimental report [36]. Further, we find that these low frequency modes travel nearly unimpeded through the interface, maintaining their wave vectors on each side of the interface. Our work shows that even completely disordered regions may not be effective at reflecting THz phonons, with implications for efforts to alter thermal conductivity in nanocrystalline solids.

II. THEORY

A. Mode-resolved AGF formalism

The mode-resolved AGF formalism has been reported in Refs. [32,33] in detail. Here, we briefly review the formalism for calculating phonon modal transmission coefficients. In the framework of AGF [21,22], the system is divided into three interacting parts: the left and right semi-infinite leads and the device indicated by the blue dashed lines, as depicted in Fig. 1. The equations of motion of this system can be written by the following matrix form:

$$(\omega^2 \mathbf{I} - \mathbf{H})\Psi = 0, \tag{1}$$

where ω is the radial frequency, $\mathbf{I}$ is the identity matrix, Ψ are the eigenvectors of the total system, and $\mathbf{H}$ is the dynamical matrix representing the atomic interactions

$$\mathbf{H} = \begin{bmatrix} \ddots & \ddots & \ddots & & & \\ \ddots & \mathbf{H}_L^{11} & \mathbf{H}_L^{01} & \mathbf{0} & & \\ \ddots & \mathbf{H}_L^{10} & \mathbf{H}_L^{00} & \mathbf{H}_{LD} & \mathbf{0} & \\ & \mathbf{0} & \mathbf{H}_{DL} & \mathbf{H}_D & \mathbf{H}_{DR} & \mathbf{0} \\ & & \mathbf{0} & \mathbf{H}_{RD} & \mathbf{H}_R^{00} & \mathbf{H}_R^{01} & \ddots \\ & & & \mathbf{0} & \mathbf{H}_R^{10} & \mathbf{H}_R^{11} & \ddots \\ & & & & \ddots & \ddots & \ddots \end{bmatrix}, \tag{2}$$

where $\mathbf{H}_D$ is the dynamical matrix of the device, $\mathbf{H}_{LD}$ is the coupling matrix between the left lead and the device, and $\mathbf{H}_{DR}$ is the coupling matrix between the device and the right lead. As $\mathbf{H}$ is hermitian, $\mathbf{H}_{LD} = \mathbf{H}_{DL}^\dagger$ and $\mathbf{H}_{RD} = \mathbf{H}_{DR}^\dagger$. The left lead is divided into two sublayers, which is indicated by red dashed lines in Fig. 1. Correspondingly, the dynamical matrix of the left lead $\mathbf{H}_L$ is divided into submatrices, where $\mathbf{H}_L^{00}$ represents the dynamical matrix of the layer in the left lead in contact with the device, $\mathbf{H}_L^{11}$ is the dynamical matrix of the layer in the left lead in contact with the previous layer, and $\mathbf{H}_L^{01}$ is the coupling matrix between them, as depicted in Fig. 1. The same notation is also used for the right lead. The device retarded

Green's function $\mathbf{G}_D^{\text{ret}}(\omega)$ is defined as

$$\mathbf{G}_D^{\text{ret}}(\omega) = (\omega^2 \mathbf{I} - \mathbf{H}_D - \Sigma_L - \Sigma_R)^{-1}. \tag{3}$$

Σ are self-energies defined as $\Sigma_L = \mathbf{H}_{DL}\mathbf{g}_L^{00}\mathbf{H}_{LD}$, $\Sigma_R = \mathbf{H}_{DR}\mathbf{g}_R^{00}\mathbf{H}_{RD}$ for the left, right leads. The left and right uncoupled retarded Green's functions $\mathbf{g}_L^{00} = [(\omega^2 + \eta i)\mathbf{I} - \mathbf{H}_L]^{-1}$, $\mathbf{g}_R^{00} = [(\omega^2 + \eta i)\mathbf{I} - \mathbf{H}_R]^{-1}$ are computed using the decimation technique [37]. The spectral transmission is calculated as

$$\Xi(\omega) = \mathbf{Tr}(\Gamma_R \mathbf{G}_D^{\text{ret}} \Gamma_L \mathbf{G}_D^{\text{ret}\dagger}) \tag{4}$$

with $\Gamma_L = i(\Sigma_L - \Sigma_L^\dagger)$ and $\Gamma_R = i(\Sigma_R - \Sigma_R^\dagger)$.

The mode-resolved AGF formalism is adapted from Ong *et al.* [32], which has been used in electronic transport [38]. The mode-resolved transmission matrix t is computed as

$$t = \frac{2i\omega}{\sqrt{a_L a_R}} \mathbf{V}_R^{1/2} [\mathbf{U}_R^{\text{ret}}]^{-1} \mathcal{G}^{\text{ret}} [\mathbf{U}_L^{\text{adv}\dagger}]^{-1} \mathbf{V}_L^{1/2}, \tag{5}$$

where $\mathcal{G}^{\text{ret}} = \mathbf{g}_R^{00}\mathbf{H}_{RD}\mathbf{G}_D^{\text{ret}}\mathbf{H}_{DL}\mathbf{g}_L^{00}$, a_L (a_R) is the length of the left (right) sublayer of lead. V_L (V_R) is the projection of the mode group velocity in the left (right) leads along the temperature gradient direction and are zero for evanescent phonons. The definition and the calculation of individual phonon modes in the left and right leads are the same as in Refs. [32] and [33]. $\Xi_{ij}^L(\omega) = |t_{ij}|^2$ provides the modal transmission for mode i in the left lead coupled with phonon j in the right lead. $\Xi_i^L(\omega) = \sum_j \Xi_{ij}^L$ is the single-mode transmission of mode i in the left lead, which is obtained by summing over all phonon modes in the right lead coupled with mode i in the left lead. $\Xi^L(\omega) = \sum_i \Xi_i^L(\omega) = \text{Tr}(t^\dagger t)$ is the spectral transmission which is the same as that in Eq. (4).

Because of translational invariance in transverse directions, we perform a Fourier transform of the equations of motion in both transverse directions, as was done in Refs. [21,32]. The transverse wave vector $\vec{k}_\parallel$ dependent transmission $\Xi(\omega, \vec{k}_\parallel)$ is defined on a two-dimensional (2D) uniform grid. The spectral transmission is

$$\Xi(\omega) = 1/N_{\vec{k}_\parallel} \sum_{\vec{k}_\parallel} \Xi(\omega, \vec{k}_\parallel), \tag{6}$$

where $N_{\vec{k}_\parallel}$ is the number of transverse wave vectors. The mode-resolved transmission matrix t is related to $\vec{k}_\parallel$ as $t(\vec{k}_\parallel)$. Therefore, the $\vec{k}_\parallel$ dependent modal transmission is

$$\Xi_{ij}^L(\omega, \vec{k}_\parallel) = |t_{ij}(\vec{k}_\parallel)|^2. \tag{7}$$

The $\vec{k}_\parallel$ dependent single-mode transmission, obtained by summing over modal transmissions of all the phonon modes in the right lead coupled with the i mode in the left lead, is

$$\Xi_i^L(\omega, \vec{k}_\parallel) = \sum_j \Xi_{ij}^L(\omega, \vec{k}_\parallel). \tag{8}$$

The transverse wave vector $\vec{k}_\parallel$ dependent transmission, obtained by summing over single-mode transmissions of all modes of a given frequency and transverse wave vector, is

$$\Xi^L(\omega, \vec{k}_\parallel) = \sum_i \Xi_i^L(\omega, \vec{k}_\parallel) = \text{Tr}(t(\vec{k}_\parallel)^\dagger t(\vec{k}_\parallel)). \tag{9}$$
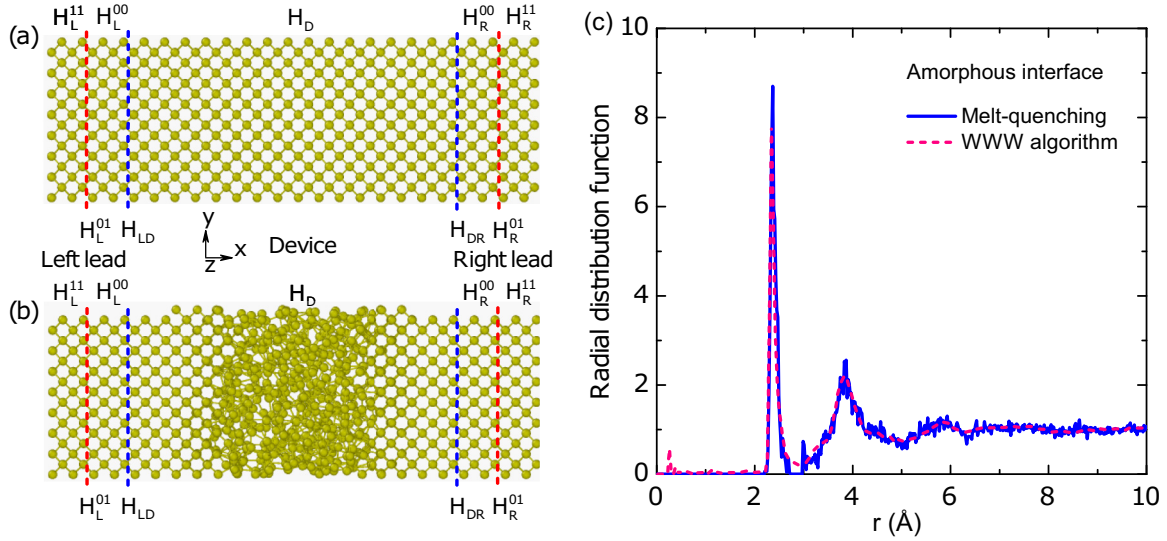
FIG. 1. (a) Crystalline Si structure with 12 uc in the x direction and 4 uc in the transverse directions (y and z directions). The blue dashed lines divide the crystalline Si into three parts: the left semi-infinite lead, device, and right semi-infinite lead. The red dashed lines divide the left (right) lead into two sublayers to enable the calculation of the longitudinal wave vectors of phonon modes. (b) Crystalline Si with amorphous Si interface. The geometry is the same as that in (a) except the device region is amorphous Si. (c) Radial distribution function $g(r)$ for atoms in the amorphous region. r is the distance between atoms. The solid blue and red dashed lines correspond to the $g(r)$ of amorphous Si interface generated by melt-quenching and WWW algorithm, respectively.

In this work, k_y and k_z are normalized by the maximum value of $\vec{k}_\parallel$, and a transverse wave-vector grid of size 20×20 is used.

Finally, the temperature dependent thermal conductance per unit area $\sigma(T)$ for the device region is calculated by the Landauer formalism:

$$\sigma(T) = \frac{1}{2\pi A} \int_0^{\omega_{\max}} \hbar\omega \frac{\partial n}{\partial T}(\omega, T) \Xi(\omega) d\omega. \qquad (10)$$

A is the transverse area and $n(\omega, T)$ is the Bose-Einstein distribution, and T is temperature.

B. Generating amorphous interface

We generate an amorphous interface using the melt-quenching method [39–41]. The melt-quenching simulations were performed by LAMMPS (large-scale atomic/molecular massively parallel simulator) code [42] with the Tersoff potential [43]. The time step is 0.5 fs, and periodic boundary conditions are applied in all directions. We begin the procedure by preparing a crystalline Si structure in Fig. 1(a). The length of the system is 12 unit cells (uc) of bulk Si. Here we set the conventional cell of Si as a unit cell and the lattice constant as 5.43 Å. The width and height are both 4 uc in the transverse directions (y and z directions), and the heat flux direction x is along the [100] direction of the conventional cell of bulk Si. The spectral transmissions of amorphous interfaces with different cross sections (3, 4, 5 uc in transverse directions) are studied and found that they are nearly identical for all the frequency range, demonstrating that our structure with 4 uc in the transverse directions yields converged results. The simulation cell is divided into three layers. The left (right) layer is divided into two equivalent sublayers with 1 uc length. Therefore, a_L and a_R both are 5.43 Å, and A is $(4 \times 5.43)^2$ Å^2. The device layer with 8 uc length is in the middle.

The atoms from 5 to 8 uc in the x direction are melted at 3600 K by Nosé-Hoover thermostat by applying NVT ensemble for 0.5 ns, then the system is quickly quenched to 1000 K at the rate of 860 K/ps. The system is annealed at 1000 K for 0.5 ns, and then it is quickly quenched to 20 K at the rate of 160 K/ps. During the melting, quenching, and annealing procedures, all other atoms are fixed. Next, we perform an equilibration for 2.5 ns in an NVT ensemble, then obtain the average atom positions over the next 2.5 ns. In the equilibration and calculation of atom position procedures, the atoms from 4 to 9 uc in the x direction are allowed to move but all other atoms are fixed. In this way, the strains between the amorphous interface and the leads are released in the regions with 1 uc thickness, which are from 4 to 5 uc and 8 to 9 uc in the x direction. We also performed calculations in which the strain was released in a 2 uc thickness region but little difference in the spectral transmissions was observed, confirming that our calculations were not affected by the size of strain release region.

Figure 1(b) shows the resulting amorphous interface. The radial distribution function $g(r)$ for atoms in the amorphous interfaces generated by melt-quenching method is calculated and presented in Fig. 1(c). For comparison, we also show the $g(r)$ of amorphous Si generated from the modified Wooten-Winer-Weaire (WWW) algorithm, provided by N. Mousseau [44]. Our results agree well with the function from Ref. [40], indicating the region is indeed amorphous.

After the amorphous interface is generated, force constants of the system are calculated by lattice dynamics (LD) using the general utility lattice program (GULP) [45]. We set the neighbors searching cutoff to 4.4 Å while constructing the harmonic matrix so that all the interacting atoms in the Tersoff potential are included. As the AGF method solved by decimation technique requires that only adjacent layers have interactions,
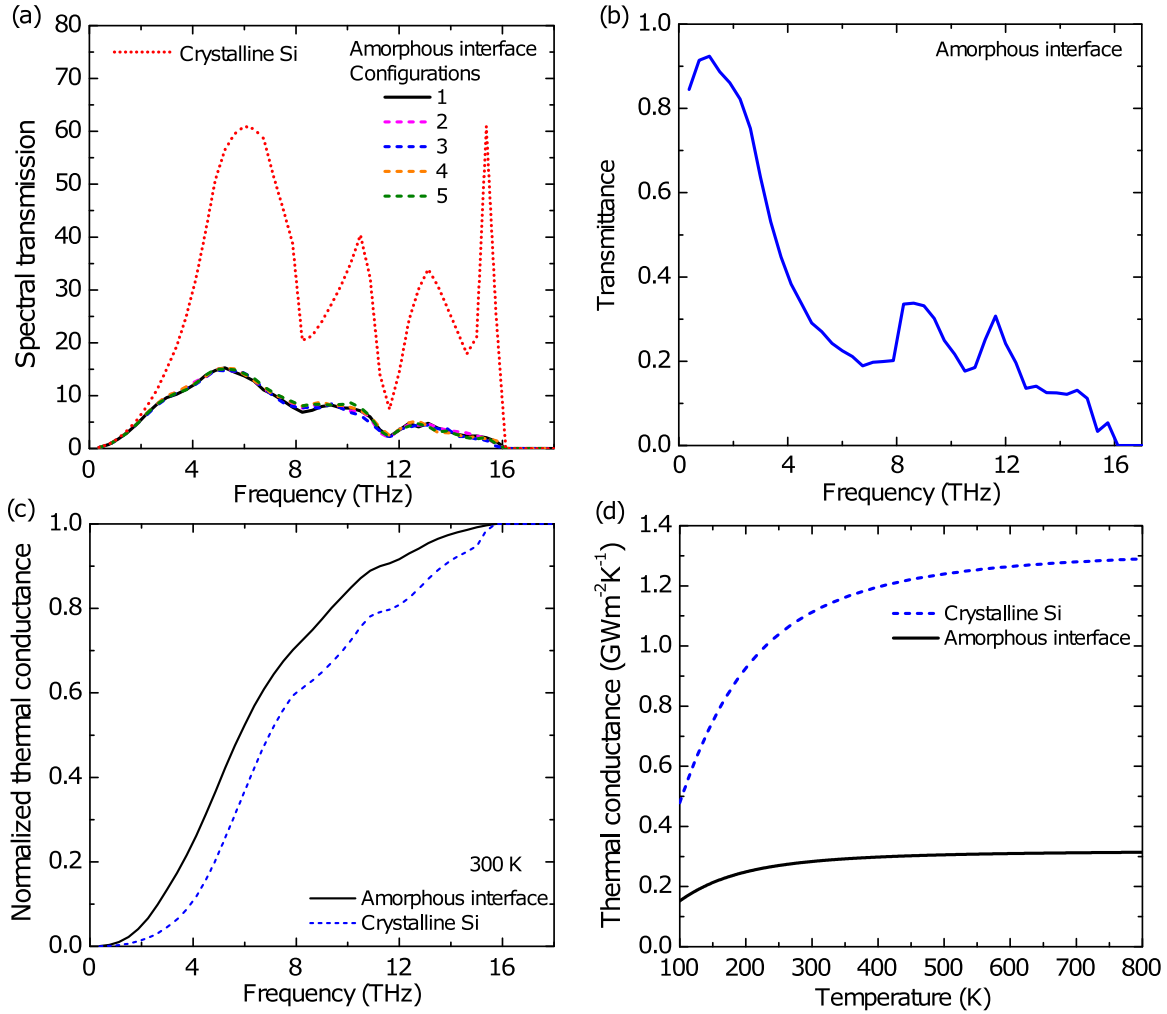
FIG. 2. (a) Spectral transmission for crystalline Si (red dotted line) and amorphous Si interfaces created in separate melt-quenching procedures (solid black and dashed pink, blue, yellow, and green lines) versus phonon frequency. The thickness of aSi interfaces is 4 uc (21.72 Å). The spectral transmission is nearly identical for all the aSi interfaces. (b) Transmittance of amorphous Si interface versus phonon frequency. (c) Normalized accumulated thermal conductance versus frequency at 300 K for cSi (blue dashed line) and aSi (black line) interfaces. (d) Thermal conductance of the device region versus temperature for cSi (blue dashed line) and aSi (black line) interfaces.

we set the length as 1 uc for the sublayers in the left and right leads, as shown in Figs. 1(a) and 1(b).

III. RESULTS

A. Spectral transmission at aSi interface

We first plot the spectral transmission, $\Xi(\omega)$, for crystalline Si and amorphous Si interfaces in Fig. 2(a). The figure shows that the spectral transmission is reduced compared to that of the crystalline silicon interface for phonons with frequency larger than 2 THz. To investigate if the configurations of amorphous interfaces affect phonon transmission, we generated five different aSi interface by setting different initial conditions in the melt-quenching procedure. The spectral transmissions for different configurations are presented in Fig. 2(a) and are nearly identical. We therefore select one of these configurations for subsequent analysis. The nearly identical spectral transmissions of Fig. 2(a) suggest that our conclusions generally apply to amorphous Si interfaces, but a larger number of calculations should be performed to fully verify this assertion.

The transmittance is defined as:

$$\tau = \Xi(\omega)_{aSi} / \Xi(\omega)_{cSi}. \tag{11}$$

It describes the fraction of incident phonons at frequency ω that is transmitted compared to that of the perfect crystalline domain. $\Xi(\omega)_{aSi}$ and $\Xi(\omega)_{cSi}$ refer to spectral transmission for the amorphous Si and crystalline Si domains, respectively. This calculation thus produces a transmission coefficient averaged over all phonon modes of the same frequency. Figure 2(b) shows the phonon transmittance for an amorphous interface. The phonon transmittance rapidly decreases when frequency increases from 2 to 4 THz, and when the frequency is larger than 12 THz, the transmittance is less than 0.2. Phonons with frequency less than 3 THz have transmittance larger than 0.64, while the transmittance is less than 0.4 with frequency larger than 4 THz. The trend of transmittance is consistent with prior simulation works [30,31]. Interestingly, our calculation is also quite compatible with our recent experimental measurement of transmission coefficients for an Al/Si interface [36], which
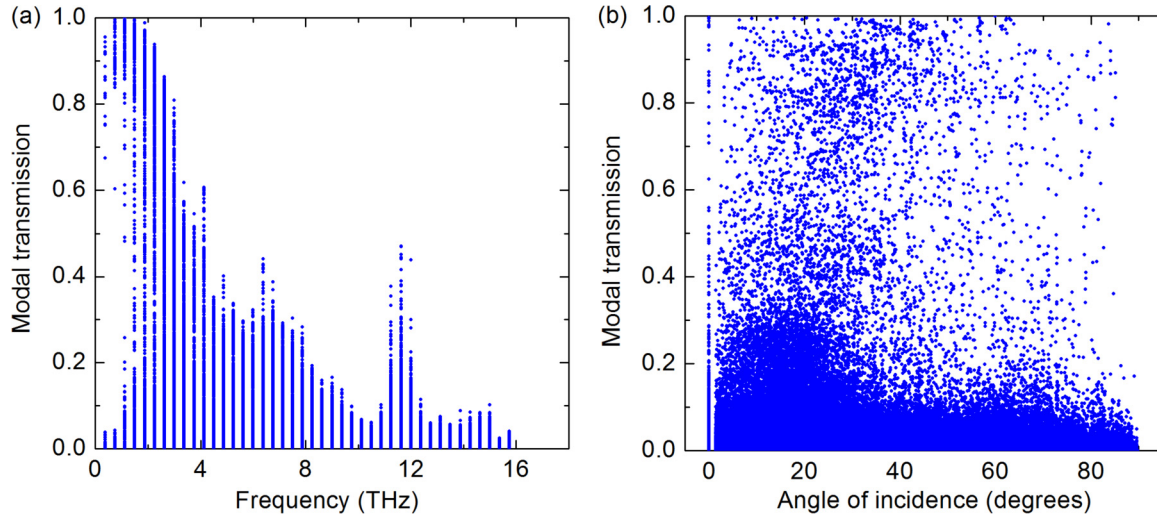
FIG. 3. Modal transmission coefficients, $\Xi_{ij}^L(\omega,\vec{k}_\parallel)$, versus frequency (a) and angle of incidence (b) for the amorphous Si interface. Transmission coefficients are near unity for frequencies less than 3 THz and decrease to near zero as frequency increases. Little dependence on incidence angle is observed.

also exhibited a similar trend of decreasing transmission coefficients with increasing phonon frequency.

Based on spectral transmission, thermal conductance of amorphous Si and crystalline Si interfaces can be calculated using Eq. (10). Figure 2(c) shows the normalized accumulation of thermal conductance at 300 K. Due to the reduction of transmission for the amorphous interface, phonons with frequency less than 6 THz contribute 52% to the total thermal conductance of amorphous Si interface while they contribute 36% for crystalline Si. We also calculate the thermal conductance from 100 to 800 K, shown in Fig. 2(d). The thermal conductance of the device region containing the amorphous interface (σ_{aSi}) is greatly decreased compared with that of the crystalline Si domain (σ_{cSi}). For example, σ_{cSi} is reduced from 1.11 GWm^{-2} K^{-1} to $\sigma_{aSi} = 0.28$ GWm^{-2} K^{-1}, a 75% reduction at 300 K.

B. Analysis of modal transmission

We now examine the modal dependence of the transmission coefficients for the amorphous interface. We plot modal transmission, $\Xi_{ij}^L(\omega,\vec{k}_\parallel)$, for all incident phonons in the left lead to transmitted phonons in the right lead in Fig. 3. Figure 3(a) shows that the maximum value of phonon modal transmission decreases as frequency increases. The transmission coefficients at frequency below around 3 THz are near unity. The near zero transmission coefficients at these frequencies correspond to mode-conversion processes that are forbidden at normal incidence and are unlikely at slightly off-normal incidence. For frequencies larger than around 12 THz, the transmission coefficients are less than 0.1.

The modal AGF formalism also allows us to investigate the dependence of transmission coefficients on angle of incidence. The results are given in Fig. 3(b). We observe little dependence on incidence angle, which may be expected due to the atomic-scale disorder of the amorphous region.

We further examine the single-mode transmission $\Xi_i^L(\omega,\vec{k}_\parallel)$, or the summation of modal transmissions for

all modes in the right lead coupled with the mode in the left lead, for the amorphous interface by plotting the dispersion of the supercell (sublayer in Fig. 1). The single-mode transmission for all normally incident modes is shown in Fig. 4(a). The color represents the value of single-mode transmission according to the color bar. The figure confirms the prior observations that acoustic modes with frequencies up to 3 THz transmit the interface nearly unimpeded. Most other modes with higher frequencies are highly reflected, with the exception of certain zone-center modes around 11 THz that have single-mode transmission around 0.4.

The modal transmissions for normally incident phonons are also shown in Fig. 4(b). For crystalline Si interface, mode conversion of normally incident longitudinal phonons is not allowed under the harmonic approximation in the mode-resolved AGF method. For the amorphous interface, at the low frequency of 0.375 THz the longitudinal mode primarily transmits to the same mode [$\Xi_{ii}^L(\omega,\vec{k}_\parallel) = 0.9212$] but mode conversion to the transverse modes is possible although unlikely [$\Xi_{ij}^L(\omega,\vec{k}_\parallel) = 4.0 \times 10^{-4}$ and 0.0268]. The single-mode transmission for the longitudinal mode, $\Xi_i^L(\omega,\vec{k}_\parallel)$, is therefore 0.9484. Figure 4(c) compares the spectral transmission for amorphous interfaces and crystalline Si interface only including the normal incident modes. Generally, the transmission is reduced for the amorphous interface except below around 3 THz.

We next examine the wave-vector dependent transmission $\Xi^L(\omega,\vec{k}_\parallel)$, which is the summation of single-mode transmissions of all the phonon modes at a given frequency and transverse wave vector, for the amorphous interface. For a specific frequency, the $\vec{k}_\parallel$ dependent transmission has a distribution on 2D uniform $\vec{k}_\parallel$ grid. To investigate the change of $\Xi^L(\omega,\vec{k}_\parallel)$ at each $\vec{k}_\parallel$, we calculated the ratio of $\vec{k}_\parallel$ dependent transmission for aSi interface to that for cSi interface, $\Xi^L(\omega,\vec{k}_\parallel)_{aSi} / \Xi^L(\omega,\vec{k}_\parallel)_{cSi}$, which is shown in Fig. 5.

In Fig. 5(a), the frequency is 0.375 THz; we find that ratio of $\vec{k}_\parallel$ dependent transmission is maximum at normal
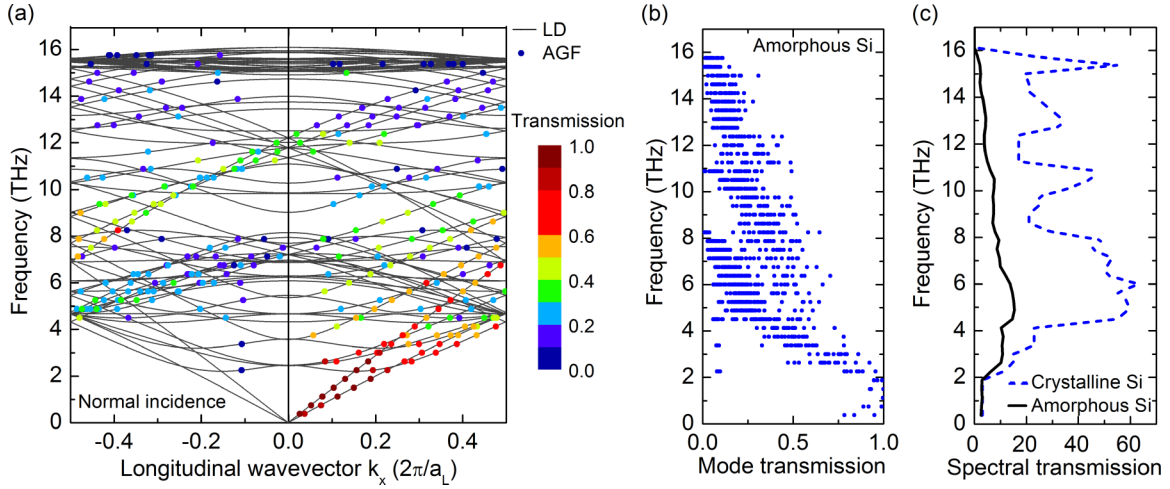
FIG. 4. (a) Phonon single-mode transmission, $\Xi_i^L(\omega, \vec{k}_{\parallel})$, plotted in the folded Brillouin zone of the supercell (sublayer in Fig. 1) for normal incidence phonons ($k_y = 0$, $k_z = 0$) in the left lead for the amorphous Si interface. The dashed black line is the phonon dispersion calculated by lattice dynamics (LD) implemented in GULP [45]. The solid dots are the phonon modes calculated by AGF, and the color represents the value of single-mode transmission, $\Xi_i^L(\omega, \vec{k}_{\parallel})$, according to the color bar. (b) Phonon modal transmission, $\Xi_{ij}^L(\omega, \vec{k}_{\parallel})$, for all the normally incident phonons in the left lead for the amorphous Si interface. (c) Spectral transmission, $\Xi(\omega) = 1/N_{\vec{k}_{\parallel}} \sum_{\vec{k}_{\parallel}} \Xi(\omega, \vec{k}_{\parallel})$, with $k_y = 0$ and $k_z = 0$, only including the normally incident phonons in the left lead for the amorphous Si interface (black line) and crystalline Si interface (blue dashed line). Phonon modes with frequencies up to 3 THz transmit the interface nearly unimpeded.

incidence and gradually decreases when k_x and k_y increase. For sufficiently large transverse wave vectors, no mode exists with the specified frequency. In Fig. 5(b), the frequency is 15.375 THz, the maximum and minimum transmission ratios are 0.039 and 0.030, respectively, which indicates that $\vec{k}_{\parallel}$ dependent transmission is nearly independent of wave vector and much less than unity.

C. Role of thickness of aSi interface

Thus far, our calculations have shown that phonons with frequency less than around 3 THz and close to normal incidence transmit through the amorphous interface largely

unimpeded. It is interesting to consider whether this effect is altered by the thickness of the amorphous region. We generate interfaces with 4, 5, and 6 uc thickness using the same melt-quenching procedure. The spectral transmission curves of these three interfaces are shown in Fig. 6(a). Overall, phonon transmission is reduced as thickness of amorphous Si increases, but low frequency phonon transmission remains nearly identical, suggesting that the amorphous region supports propagating waves of frequencies less than 3 THz.

We also computed the thermal conductance versus temperature for each device region in Fig. 6(b). The thermal conductance is also reduced when thickness increases, but at low temperature (below 200 K) the reduction is relatively small. This
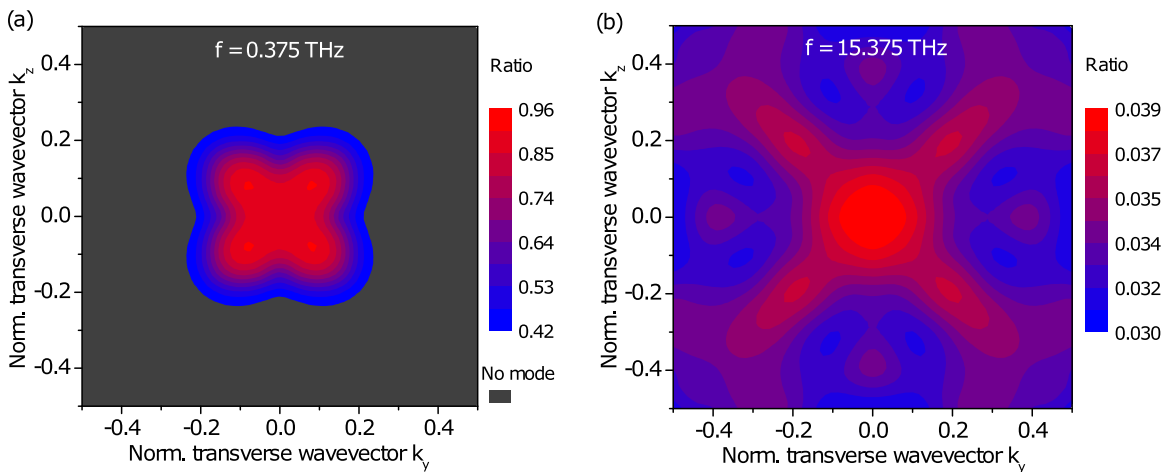

FIG. 5. Distribution of the ratio of $\vec{k}_{\parallel}$ dependent transmission for aSi interface to that at the cSi interface, $\Xi^L(\omega, \vec{k}_{\parallel})_{aSi} / \Xi^L(\omega, \vec{k}_{\parallel})_{cSi}$ on a uniform $\vec{k}_{\parallel}$ grid for (a) 0.375 THz and (b) 15.375 THz. k_y and k_z are normalized by $2\pi/a_T$, where a_T is the width of the leads. The color represents the value of ratio according to the color bars. The gray color indicates that no phonon modes exist for the given frequency and wave vector.
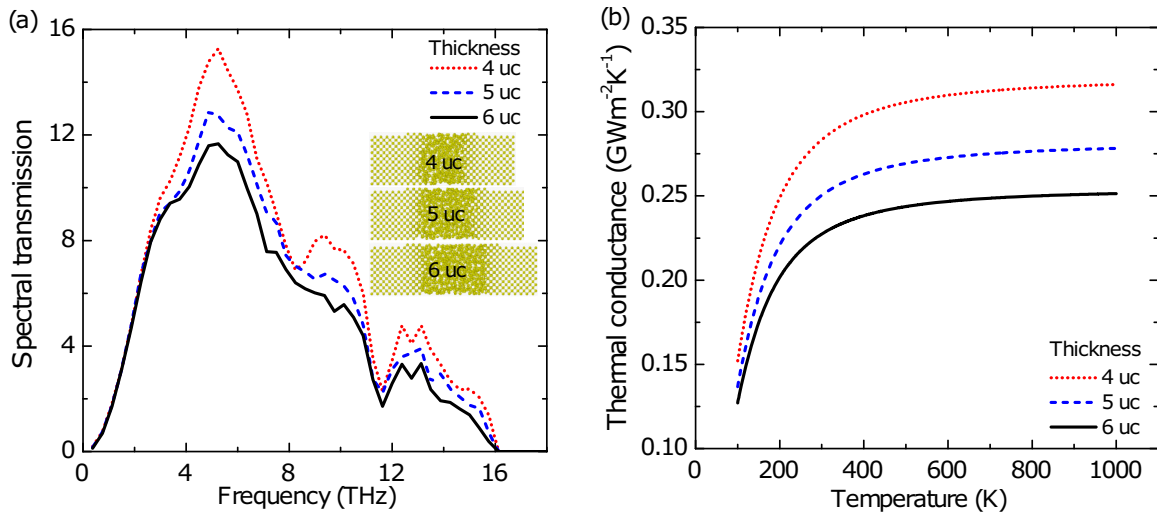
FIG. 6. (a) Spectral transmission for 4 (red dotted line), 5 (blue dashed line), and 6 (black line) uc thickness aSi interfaces versus frequency. The inset shows the structures of aSi interface with different thickness. (b) Thermal conductance of aSi interfaces of different thickness, 4 (red dotted line), 5 (blue dashed line), and 6 (black line) uc, versus temperature. Phonon transmission is reduced as thickness of amorphous Si increases, but low frequency phonon transmission remains nearly unchanged.

observation is because low frequency phonons make the dominant contribution to thermal conductance at low temperature, which have little reduction of transmission as shown in Fig. 6(a).

D. Specularity of aSi interface

Finally, we investigate the specularity of the transmission process. As the phonons transmit through the interface, they may preserve their wave vector in a specular transmission process or they may be transmitted in a random direction due to atomic disorder. In the former process, the mode transmits the interface almost as if the interface were not present.

In conventional AGF, the specularity of interfaces cannot be calculated because the method provides the overall transmission for all phonons at a specific frequency. Taking

advantage of mode-resolved AGF, specularity can be obtained by analyzing phonon modal transmission. Recalling that the transverse wave vectors are fixed, we define a process to be specular if the difference of k_x and v_{gx} between the transmitted phonon and incident phonon are both less than 10^{-5}. Using this criterion, we calculated the specularity for the crystalline Si domain and confirmed it to be unity for all modes.

We next computed the specularity for the amorphous interface. The spectral transmission for only specular processes is shown in Fig. 7(a). For comparison, the spectral transmission for the amorphous interface in Fig. 2(a), which includes all transmission processes, is also given in Fig. 7(a). The figure shows that specular phonon transmission processes dominate the total transmission below about 3 THz.
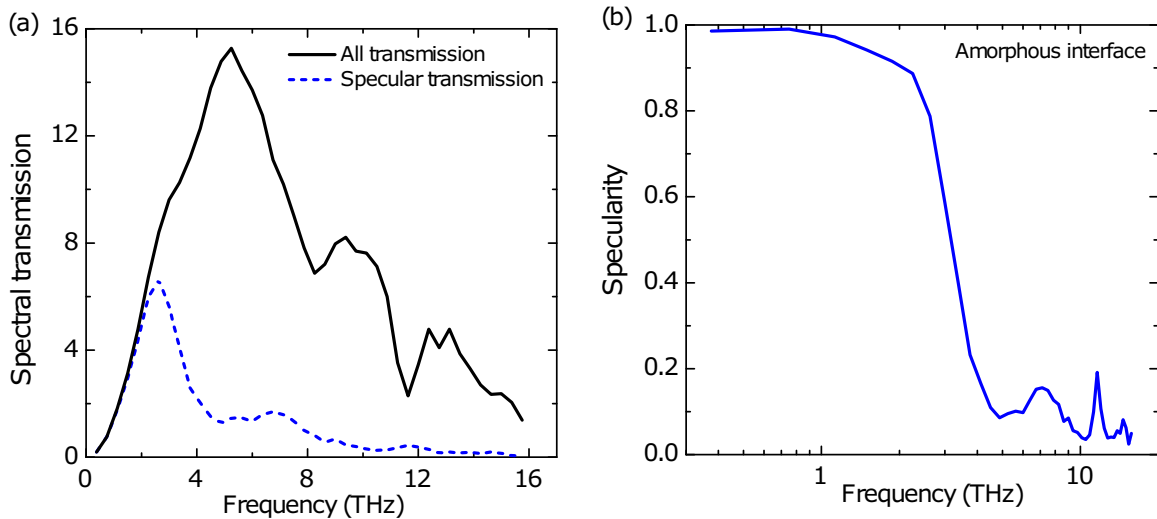

FIG. 7. (a) Spectral transmission including all transmission process (black line) and only including specular transmission processes (blue dashed line) versus frequency. (b) Specularity of aSi interface versus frequency. Specular phonon transmission processes dominate the total transmission below about 3 THz.

For these calculations, we define specularity as the ratio of spectral transmission only including specular transmission processes to that including all transmission processes. The result is shown in Fig. 7(b). At low frequency (less than 2 THz), the specularity is larger than 0.9 and rapidly decreases as frequency increases from 2 to 4 THz. When frequency is less than 3 THz, the specularity is larger than 0.6, while the specularity is smaller than 0.2 with frequency larger than 4 THz. These results further confirm that phonons of frequency less than around 3 THz transmit the amorphous region essentially unimpeded, even maintaining their wave vector as they transmit. This conclusion is in agreement with a prior experiment measurement of transmission coefficients at an Al/Si interface [36]. Our results have implications for manipulating the thermal conductivity of nanocrystalline solids as grain boundaries with structures like those studied here are unlikely to be effective in reflecting low frequency modes.

IV. CONCLUSION

We investigated phonon modal transmission using the mode-resolved AGF for an aSi interface between two crystalline Si leads. We find that the interface acts as a low-pass filter, reflecting modes of frequency greater than around 3 THz while transmitting those below this frequency. Further, we find that these low frequency modes travel nearly unimpeded through the interface, even maintaining their wave vectors as they transmit. In addition, the thickness of amorphous interface has little effect on transmission of low frequency phonons. Our work shows that even completely disordered regions may not be effective at reflecting THz phonons, with implications for efforts to alter thermal conductivity in nanocrystalline solids.

[1] D. G. Cahill, P. V. Braun, G. Chen, D. R. Clarke, S. Fan, K. E. Goodson, P. Keblinski, W. P. King, G. D. Mahan, A. Majumdar *et al.*, Appl. Phys. Rev. **1**, 011305 (2014).

[2] R. Prasher, Proc. IEEE **94**, 1571 (2006).

[3] E. T. Swartz and R. O. Pohl, Rev. Mod. Phys. **61**, 605 (1989).

[4] D. G. Cahill, Rev. Sci. Instrum. **75**, 5119 (2004).

[5] W. A. Little, Can. J. Phys. **37**, 334 (1959).

[6] A. Maiti, G. D. Mahan, and S. T. Pantelides, Solid State Commun. **102**, 517 (1997).

[7] M. Hu, P. Keblinski, and P. K. Schelling, Phys. Rev. B **79**, 104305 (2009).

[8] Y. Wang, X. Ruan, and A. K. Roy, Phys. Rev. B **85**, 205311 (2012).

[9] E. S. Landry and A. J. H. McGaughey, Phys. Rev. B **80**, 165304 (2009).

[10] Y. Chalopin, K. Esfarjani, A. Henry, S. Volz, and G. Chen, Phys. Rev. B **85**, 195302 (2012).

[11] N. Yang, T. Luo, K. Esfarjani, A. Henry, Z. Tian, J. Shiomi, Y. Chalopin, B. Li, and G. Chen, J. Comput. Theor. Nanosci. **12**, 168 (2015).

[12] K. Gordiz and A. Henry, New J. Phys. **17**, 103002 (2015).

[13] K. Gordiz and A. Henry, Sci. Rep. **6**, 23139 (2016).

[14] Y. Zhou and M. Hu, Phys. Rev. B **95**, 115313 (2017).

[15] T. Luo and J. R. Lloyd, Adv. Funct. Mater. **22**, 2495 (2012).

[16] K. Sääskilahti, J. Oksanen, J. Tulkki, and S. Volz, Phys. Rev. B **90**, 134312 (2014).

[17] P. K. Schelling, S. R. Phillpot, and P. Keblinski, Appl. Phys. Lett. **80**, 2484 (2002).

[18] C. Kimmer, S. Aubry, A. Skye, and P. K. Schelling, Phys. Rev. B **75**, 144105 (2007).

[19] D. A. Young and H. J. Maris, Phys. Rev. B **40**, 3685 (1989).

[20] H. Zhao and J. B. Freund, J. Appl. Phys. **97**, 024903 (2005).

[21] W. Zhang, T. S. Fisher, and N. Mingo, ASME J. Heat Transfer **129**, 483 (2007).

[22] W. Zhang, T. S. Fisher, and N. Mingo, Numer. Heat Transfer, Part B **51**, 333 (2007).

[23] N. Mingo and L. Yang, Phys. Rev. B **68**, 245406 (2003).

[24] D. A. Stewart, I. Savic, and N. Mingo, Nano Lett. **9**, 81 (2008).

[25] S. Ju, T. Shiga, L. Feng, Z. Hou, K. Tsuda, and J. Shiomi, Phys. Rev. X **7**, 021024 (2017).

[26] S. Sadasivam, N. Ye, J. P. Feser, J. Charles, K. Miao, T. Kubis, and T. S. Fisher, Phys. Rev. B **95**, 085310 (2017).

[27] C. S. Lent and D. J. Kirkner, J. Appl. Phys. **67**, 6353 (1990).

[28] S. Datta, *Quantum Transport: Atom to Transistor* (Cambridge University Press, Cambridge, 2005).

[29] M. Luisier, A. Schenk, W. Fichtner, and G. Klimeck, Phys. Rev. B **74**, 205323 (2006).

[30] X. Li and R. Yang, Phys. Rev. B **86**, 054305 (2012).

[31] Z. Tian, K. Esfarjani, and G. Chen, Phys. Rev. B **86**, 235304 (2012).

[32] Z.-Y. Ong and G. Zhang, Phys. Rev. B **91**, 174302 (2015).

[33] B. Latour, N. Shulumba, and A. J. Minnich, Phys. Rev. B **96**, 104310 (2017).

[34] R. R. Kakodkar and J. P. Feser, J. Appl. Phys. **118**, 094301 (2015).

[35] S. Sadasivam, U. V. Waghmare, and T. S. Fisher, Phys. Rev. B **96**, 174302 (2017).

[36] C. Hua, X. Chen, N. K. Ravichandran, and A. J. Minnich, Phys. Rev. B **95**, 205423 (2017).

[37] M. P. L. Sancho, J. M. L. Sancho, and J. Rubio, J. Phys. F **15**, 851 (1985).

[38] P. A. Khomyakov, G. Brocks, V. Karpan, M. Zwierzycki, and P. J. Kelly, Phys. Rev. B **72**, 035450 (2005).

[39] M. Ishimaru, S. Munetoh, and T. Motooka, Phys. Rev. B **56**, 15133 (1997).

[40] J. M. Larkin and A. J. H. McGaughey, Phys. Rev. B **89**, 144303 (2014).

[41] I. Štich, R. Car, and M. Parrinello, Phys. Rev. B **44**, 11092 (1991).

[42] S. Plimpton, J. Comput. Phys. **117**, 1 (1995).

[43] J. Tersoff, Phys. Rev. B **39**, 5566 (1989).

[44] G. T. Barkema and N. Mousseau, Phys. Rev. B **62**, 4985 (2000).

[45] J. D. Gale and A. L. Rohl, Mol. Simul. **29**, 291 (2003).